A Case Study of the Physical Processes Associated with the Atmospheric River Initial-Condition Sensitivity from an Adjoint Model

REUBEN DEMIRDJIAN

Center for Western Weather and Water Extremes, Scripps Institution of Oceanography, University of California, San Diego, La Jolla, California

JAMES D. DOYLE AND CAROLYN A. REYNOLDS

Marine Meteorology Division, Naval Research Laboratory, Monterey, California

JOEL R. NORRIS, ALLISON C. MICHAELIS, AND F. MARTIN RALPH

Center for Western Weather and Water Extremes, Scripps Institution of Oceanography, University of California, San Diego, La Jolla, California

(Manuscript received 6 June 2019, in final form 29 October 2019)

ABSTRACT

Analysis of a strong landfalling atmospheric river is presented that compares the evolution of a control simulation with that of an adjoint-derived perturbed simulation using the Coupled Ocean–Atmosphere Mesoscale Prediction System. The initial-condition sensitivities are optimized for all state variables to maximize the accumulated precipitation within the majority of California. The water vapor transport is found to be substantially enhanced at the California coast in the perturbed simulation during the time of peak precipitation, demonstrating a strengthened role of the orographic precipitation forcing. Similarly, moisture convergence and vertical velocities derived from the transverse circulation are found to be substantially enhanced during the time of peak precipitation, also demonstrating a strengthened role of the dynamic component of the precipitation.

Importantly, both components of precipitation are associated with enhanced latent heating by which (i) a stronger diabatically driven low-level potential vorticity anomaly strengthens the low-level wind (and thereby the orographic precipitation forcing), and (ii) greater moist diabatic forcing enhances the Sawyer–Eliassen transverse circulation and thereby increases ascent and dynamic precipitation. A Lagrangian parcel trajectory analysis demonstrates that a positive moisture perturbation within the atmospheric river increases the moisture transport into the warm conveyor belt offshore, which enhances latent heating in the perturbed simulation. These results suggest that the precipitation forecast in this case is particularly sensitive to the initial moisture content within the atmospheric river due to its role in enhancing both the orographic precipitation forcing and the dynamic component of precipitation.

1. Introduction

The predictability of atmospheric rivers (ARs) is vitally important for the management of water resources in California (CA) since it is a densely populated region and highly dependent on the arrival, or lack thereof, of just a handful of precipitation events per year (Dettinger 2013; Ralph et al. 2013; Dettinger and Cayan 2014; Ralph 2017; Lamjiri et al. 2017, 2018). DeFlorio et al. (2018) performed an assessment of global ARs and found that at a 2-day lead time, fewer than 75% of the European Centre for Medium-Range Weather Forecasts (ECMWF) ensemble members predicted ARs within 250 km of the actual landfall location, thus motivating the need for forecast improvements in not only the magnitude of the water vapor content in the AR, but also its position. The demand from California water managers for more accurate predictions of both AR strength and landfall position has focused attention on improving numerical

Denotes content that is immediately available upon publication as open access.

Supplemental information related to this paper is available at the Journals Online website: https://doi.org/10.1175/JAS-D-19-0155.s1.

Corresponding author: Reuben Demirdjian, rdemirdjian@ucsd.edu

DOI: 10.1175/JAS-D-19-0155.1

prediction systems, as well as aspects of the initial conditions that impact AR characteristics. A version of the Weather Research and Forecasting (WRF) Model tailored for the needs of the U.S. West Coast and employed for real-time weather forecasts by Martin et al. (2018) demonstrated improved forecast skill over the Global Forecast System (GFS) for 15 landfalling events in CA. Improvements in the initial conditions are being made in part through the AR Reconnaissance (AR-Recon) program, which targets ARs using airborne instruments, having an emphasis on the in situ dropsondes (Ralph 2018). The optimal aircraft tracks and dropsondes' locations, however, are typically a matter for debate because it is not always clear where additional observations are most likely to improve the analyses and subsequent forecasts. This study focuses on improving the dynamical understanding of how perturbations identified using an adjoint technique grow rapidly and impact AR forecasts.

It has long been understood that small errors in the initial conditions can grow rapidly due to the chaotic nature of the atmosphere (Lorenz 1969). However, an initial-condition error of a state variable can have a range of downstream impacts depending on how it projects onto fast-growing perturbations (e.g., Reynolds et al. 2001, 2019; Doyle et al. 2014). Atmospheric instabilities are the vehicles through which small errors in the initial state may grow rapidly, thereby contributing toward forecast errors. Aircraft reconnaissance is often utilized to reduce the initial-condition errors during impactful weather phenomena by collecting in situ observations of critical regions where there may otherwise be gaps in the observing systems (Shoemaker et al. 1990; Gray et al. 1991; Martin and Gray 1993; Majumdar 2016). However, the optimal sampling locations providing the greatest improvement to the forecast are often not obvious.

The Naval Research Laboratory (NRL) Coupled Ocean–Atmosphere Mesoscale Prediction system (COAMPS) including its moist adjoint model (Amerault et al. 2008; Doyle et al. 2012, 2014) was run in real time during AR-Recon in 2018 and 2019 to provide an objective method for determining where short-term forecasts of precipitation over the west coast of North America are most sensitive to changes in the initial state. Although not always the case, the regions highlighted by the moist adjoint tool are often broadly consistent with the forecaster's dynamical understanding of phenomena that would impact the forecast evolution. By comparing dropsondes with short-range forecasts, Lavers et al. (2018) found relative errors of about 20% in the water vapor transport within ARs present in the ECMWF forecast prediction system. Since water vapor transport is highly correlated with orographic precipitation (Alpert 1986; Neiman et al. 2002, 2009; Lu et al. 2018; Ralph et al. 2013), this suggests that aircraft reconnaissance sampling should be focused in regions of strongest water vapor transport. However, there is evidence that multiple dynamical features on a variety scales may have comparable impact on precipitation forecasts. For example, Zhang et al. (2019) found that ARs are linked to a parent extratropical cyclone (EC) 80% of the time, suggesting that increased observations, and more accurate analyses, of the dynamically active regions associated with the development of the EC are also important (Zheng et al. 2013). A dynamical investigation of the sensitivity results and subsequent perturbation growth will both increase understanding of the physical mechanisms that modify AR evolution and provide context for the use of sensitivity tools for AR-Recon observing strategies.

The present study is motivated by, and complimentary to, Reynolds et al. (2019), which used the NRL moist adjoint modeling system to evaluate the sensitivity of AR forecasts for January and February 2017. They found that both the accumulated precipitation and the low-level kinetic energy forecast were most sensitive to errors in and around the AR. Furthermore, they showed that the largest forecast sensitivities are from the AR moisture content, followed by temperature and winds, consistent with the results of Doyle et al. (2014) and Doyle et al. (2019) for Atlantic ECs. Finally, they demonstrated that the strength of the initial-condition sensitivities correlates well with forecast errors, leading the authors to conclude that the moist adjoint is relevant for predictability and targeted observation applications.

The goal of the present study is to investigate the physical processes responsible for the rapid growth of perturbations derived from a moist adjoint model for an extreme landfalling AR. Out of many different landfalling AR candidates, the 7–9 January 2017 event is investigated because it occurred during the record-breaking precipitation year for Northern California and contained several interesting dynamical features, including a mesoscale frontal wave (Bjerknes and Solberg 1922; Renfrew et al. 1997; Parker 1998; Rivals et al. 1998; Hewson 2009; Neiman et al. 2016; Martin et al. 2019), which is notoriously difficult to accurately forecast.

2. Methods

a. Control and adjoint run descriptions

The 7–9 January 2017 landfalling AR is simulated using the COAMPS modeling system (Hodur 1997; Doyle et al. 2014). The COAMPS model is a nonlinear, nonhydrostatic, compressible, terrain-following numerical model. Our

simulation is run on a 221 × 161 grid with a horizontal grid spacing of 40 km on a Lambert conformal grid having 70 vertical levels; output is interpolated onto a pressure grid from 1000 to 200 hPa every 25 hPa and from 200 to 50 hPa every 50 hPa. For a full description of the parameterizations and physics packages, see Doyle et al. (2012, 2019). The relatively coarse resolution of 40 km is chosen because the tangent linear approximation tends to be valid for shorter time periods as resolution becomes finer. Future work will consider higher-resolution experiments for shorter forecast intervals.

The following paragraphs describing the adjoint model closely follows the summaries given in Reynolds et al. (2016, 2019) and Doyle et al. (2014), and is fully described in Doyle et al. (2012). The COAMPS adjoint and tangent linear models (TLM) are described in detail in Amerault et al. (2008) and Doyle et al. (2012). The same physical parameterizations are used in the nonlinear, tangent linear, and adjoint models, including ice-phase microphysics as in Doyle et al. (2012, 2014, 2019; Reynolds et al. 2019). The longwave and shortwave radiative processes are included in the nonlinear forecasts but are ignored in the TLM and adjoint in order to avoid highly nonlinear components of the physics. The COAMPS forecast and adjoint systems have been used extensively in studies ranging from tropical cyclone (TC) predictability studies (Doyle et al. 2011, 2012; Reynolds et al. 2016), to the 2018 and 2019 AR-Recon field projects (Ralph 2018; Reynolds et al. 2019).

The moist adjoint system represents the sensitivity of a forecast metric J (for model state $\mathbf{x}_t$ at time t) to each component of an earlier model state $\mathbf{x}_{t_0}$ as

$$J(\mathbf{x}_t) = J\left[\mathbf{M}_{\mathrm{nl}}\left(\mathbf{x}_{t_0}\right)\right], \tag{1}$$

where J is the response function and $\mathbf{M}_{\mathrm{nl}}$ is the nonlinear model [see Errico (1997) for a description of an adjoint model]. The response function selected in this study is the 18-h accumulated precipitation averaged over the majority of California (black box in Fig. 2). The gradient of J with respect to the initial model state is given by

$$\frac{\partial J}{\partial \mathbf{x}_{t_0}} = \mathbf{M}_{\mathrm{tlm}}^{\mathrm{T}} \frac{\partial J}{\partial \mathbf{x}_t}, \tag{2}$$

where $\mathbf{M}_{\mathrm{tlm}}$ is the tangent linear model of $\mathbf{M}_{\mathrm{nl}}$ and superscript T denotes the transpose. The term $\partial J/\partial \mathbf{x}_t$ is computed through differentiation of J with respect to the model state at time t. A requirement of J is that it must be a differentiable and continuous function.

This study is focused on the comparison of the nonlinear control forecast (CTL) with that of an adjoint-derived optimally perturbed TLM following the methods of Oortwijn and Barkmeijer (1995), Rabier et al. (1996), and Errico and Raeder (1999). These initial-time perturbations based on the adjoint sensitivity are designed to grow rapidly and result in large changes to the forecast response function. The production of these optimal perturbations follows directly from that used in Doyle et al. (2012, 2014). Perturbations to the response function J are expressed as

$$J' = \sum_j \frac{\partial J}{\partial x_j} x_j', \tag{3}$$

where $\partial J/\partial x_j$ is the gradient of the response function with respect to the jth initial-state component. The jth component of the perturbation vector $\mathbf{x}'$ is optimal when defined such that

$$x_j' = \frac{s}{w_j} \frac{\partial J}{\partial x_j}, \tag{4}$$

for weights w_j. The method for calculating the weights w_j and scaling parameter s is detailed in Doyle et al. (2014). The scaling parameter, s (units of J^{-1}), is selected such that the largest perturbation of the water vapor, potential temperature, or zonal wind speed at the initial time does not exceed $1\,\mathrm{g\,kg^{-1}}$, 1 K, or $1\,\mathrm{m\,s^{-1}}$, respectively. These perturbation magnitudes are chosen such that they are comparable to, or smaller than, errors assigned to radiosonde and dropsonde observations in the data assimilation system [1 K, $1.8\,\mathrm{m\,s^{-1}}$, and 10% relative humidity at 925 hPa ($\sim$1–1.5 $\mathrm{g\,kg^{-1}}$)]. The optimal perturbations are calculated for potential temperature, the Exner pressure perturbation, mixing ratio, all wind speed components, and microphysical species.

b. *The Sawyer–Eliassen transverse circulation model*

The Sawyer–Eliassen framework is a well-known method for calculating the 2D ageostrophic circulation within a jet-front cross section. Following the methods of Sawyer (1956), Eliassen (1962), Keyser and Shapiro (1986), and Winters and Martin (2014), the Sawyer–Eliassen equation is given by

$$\left(-\gamma\frac{\partial\theta}{\partial p}\right)\frac{\partial^2\Psi}{\partial y^2} + \left(2\frac{\partial M}{\partial p}\right)\frac{\partial^2\Psi}{\partial p\,\partial y} + \left(-\frac{\partial M}{\partial y}\right)\frac{\partial^2\Psi}{\partial^2 p} = Q_g - \gamma\frac{\partial}{\partial y}\left(\frac{d\theta}{dt}\right), \tag{5}$$

where y is in the across-jet direction, x is in the along-jet direction, Ψ is the ageostrophic streamfunction, θ is potential temperature, $M = U_g - fy$ is the absolute momentum, $Q_g = 2\gamma(\partial U_g/\partial y)(\partial\theta/\partial x) + 2\gamma(\partial V_g/\partial y)(\partial\theta/\partial y)$ is the quasigeostrophic forcing term (stretching and

shearing deformations, respectively), U_g is the along-jet geostrophic wind, V_g is the across-jet geostrophic wind, $\gamma = R/fp_0(p_0/p)^{c_v/c_p}$, $p_0 = 1000\,\text{hPa}$, $c_v = 718\,\text{J kg}^{-1}\,\text{K}^{-1}$, $c_p = 1004\,\text{J kg}^{-1}\,\text{K}^{-1}$, $R = 287\,\text{J kg}^{-1}\,\text{K}^{-1}$, f is the Coriolis parameter, and $d\theta/dt$ is the diabatic heating rate. The coefficients on the LHS of Eq. (5) represent the static stability, baroclinicity, and inertial stability, respectively. The diabatic heating term is calculated following Emanuel et al. (1987) and Winters and Martin (2014), and is given by

$$\frac{d\theta}{dt} = \omega\left(\frac{\partial\theta}{\partial p} - \frac{\Gamma_m}{\Gamma_d}\frac{\theta}{\theta_e}\frac{\partial\theta_e}{\partial p}\right), \tag{6}$$

where θ_e is the equivalent potential temperature calculated following Bryan (2008), Γ_m is the moist adiabatic lapse rate, and Γ_d is the dry adiabatic lapse rate. Equation (6) was found to be in very good agreement with the direct model output of the latent heating, indicating that the diabatic heating is dominated by latent heating. We use a parameterized form for the diabatic heating because only the instantaneous latent heating rate is available from the model output, which can have some very large heating/cooling gradients and small-scale structure, thereby making it difficult for the numerical routine of Eq. (5) to converge.

Equation (5) is a second-order elliptic partial differential equation (PDE) that is solved numerically on a grid from 1000 to 100 hPa every 25 hPa in the vertical and interpolated along a transect of length 2250 km with a 45-km spacing. It is solved using the method of successive overrelaxation (SOR) in a piecewise manner for the dry (Q_g) and moist ($d\theta/dt$) forcing terms separately. The boundary conditions used are $\Psi = 0$ at all boundaries following Shapiro (1981) and Winters and Martin (2014). All cross sections were manually inspected prior to application of the SOR method to ensure that (i) the full jet–front structure is captured, and (ii) the boundary conditions were appropriate and did not neglect any important features.

c. Air parcel trajectories

Both forward and backward trajectories are utilized in this study, each calculated from 15-min output, with 25-hPa vertical spacing, on a latitude–longitude grid interpolated to 0.375° × 0.275°. The method applied to calculate both the forward and backward trajectories is a three-step process that 1) determines the three-dimensional wind components of each air parcel, 2) advances the air parcels forward by a time step, and 3) linearly interpolates to the new locations at which point steps 1 and 2 are repeated following Wernli and Davies (1997) and Wernli (1997). This method allows for an adaptable and computationally inexpensive method of estimating the parcel trajectories.

3. Case study background

a. Synoptic-scale overview

The heavy precipitation that fell in California during 7–9 January 2017 was due to a landfalling AR event reaching AR category 4 (CAT4) out of a scale of 5 (Ralph et al. 2019) having two distinct pulses or waves. At the forecast initialization time (Figs. 1a,f), AR wave 1 (labeled W1) is located ahead of the synoptic-scale cyclone's (36°N, 145°W) cold front and is thereby already associated with a mature EC having a moderate sea level pressure (SLP) minimum of about 990 hPa and large integrated vapor transport (IVT) values exceeding $800\,\text{kg s}^{-1}\,\text{m}^{-1}$. Following the eastward propagation of a short wave seen in the SLP field, the AR makes landfall in central California beginning around 1200 UTC 7 January with an IVT plume containing maximum values located offshore upward of $750\,\text{kg s}^{-1}\,\text{m}^{-1}$ (Figs. 1b,g).

A resurgence in the IVT (labeled W2) is apparent in Fig. 1c, and is associated with a developing secondary cyclone (labeled C; Fig. 1h), also termed a mesoscale frontal wave (Bjerknes and Solberg 1922; Renfrew et al. 1997; Parker 1998; Rivals et al. 1998; and Hewson 2009; Neiman et al. 2016; Martin et al. 2019). This rapid succession of events is consistent with the idea of AR families (Fish et al. 2019). The mesoscale frontal wave is found to be located not only in the left exit region of the upper-level jet (Fig. 1h), which is a region favorable for cyclone development, but also along the cold front where strong latent heating is expected. It is thought that the synergy between the forcings at upper and lower levels may be responsible for the development of the mesoscale frontal wave and its intensification into a secondary cyclone. Twelve hours later (Figs. 1d,i), after substantial development in both the SLP and IVT, W2 makes landfall as an AR CAT4 with maximum IVT values reaching $1000\,\text{kg s}^{-1}\,\text{m}^{-1}$. By the end of the forecast (Figs. 1e,j), the AR has decayed, and the mesoscale frontal wave has propagated poleward to 47°N, 130°W toward Vancouver.

The Stage-IV (Lin 2011) gridded observational 48-h accumulated precipitation for this case is shown in Fig. 2a and exhibits the greatest impacts in three regions: (i) the northern Sierra Nevada, with values upward of 200 mm (~8 in.); (ii) along the Northern California coast, with values also upward of 200 mm; and (iii) the Shasta region, with values slightly under 200 mm. While the CTL run simulates the distribution and magnitude of the Stage-IV precipitation pattern reasonably well in the

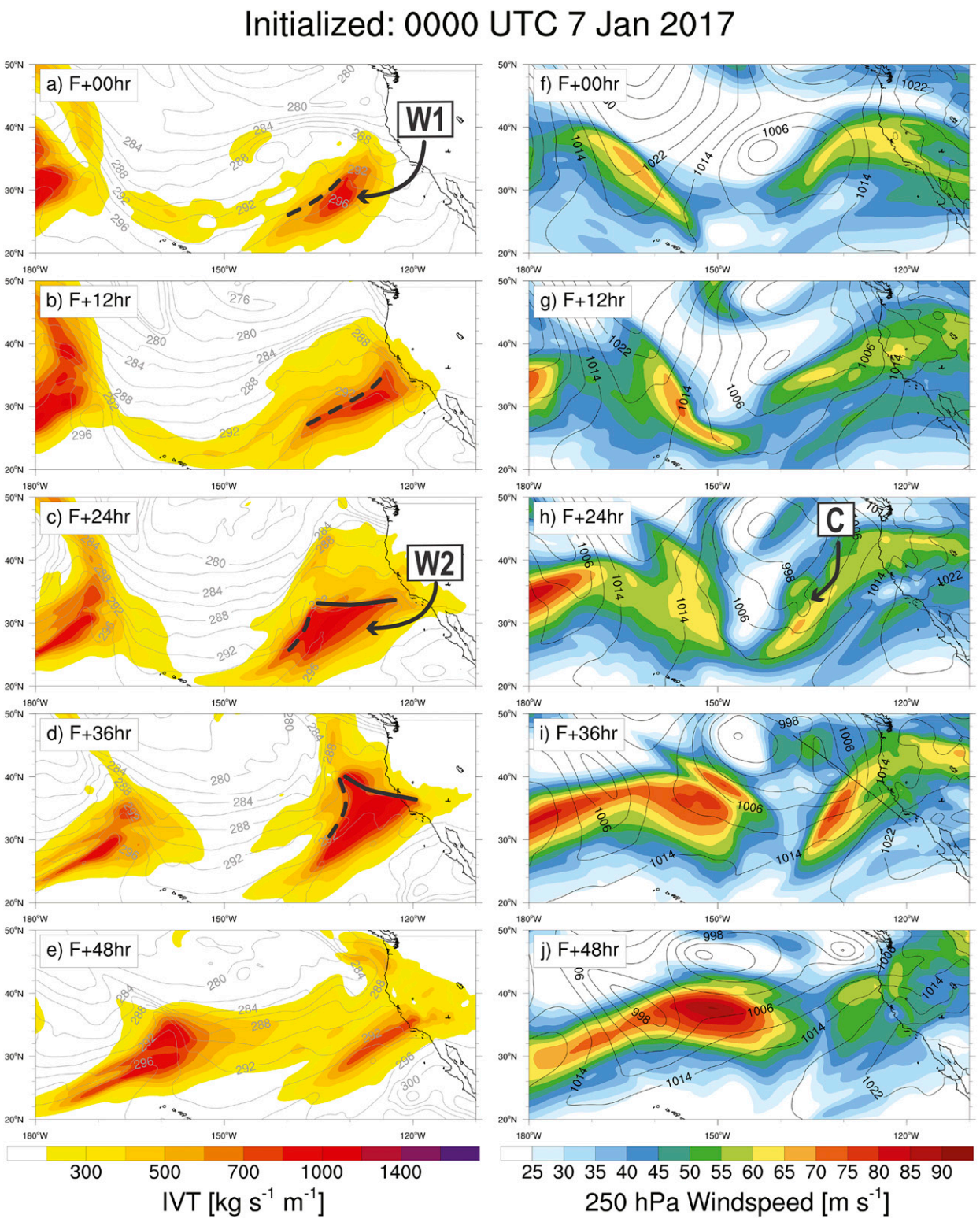

FIG. 1. Plan-view maps every 12 h of the (a)–(e) control run IVT (kg s^{-1} m^{-1}; shaded) and 925-hPa potential temperature (contour interval of 2 K; solid gray), and (f)–(j) 250-hPa wind speed (m s^{-1}) and SLP (contour interval of 4 hPa; solid black). The surface fronts are shown in (a)–(d) with the cold front in black dashed and the warm front in solid black. The location of a transect for Figs. 7–9 is shown in (i) as a solid black line. The "W1" and "W2" labels refers to different AR waves, and the "C" label refers to a developing secondary cyclone (see text for discussion).

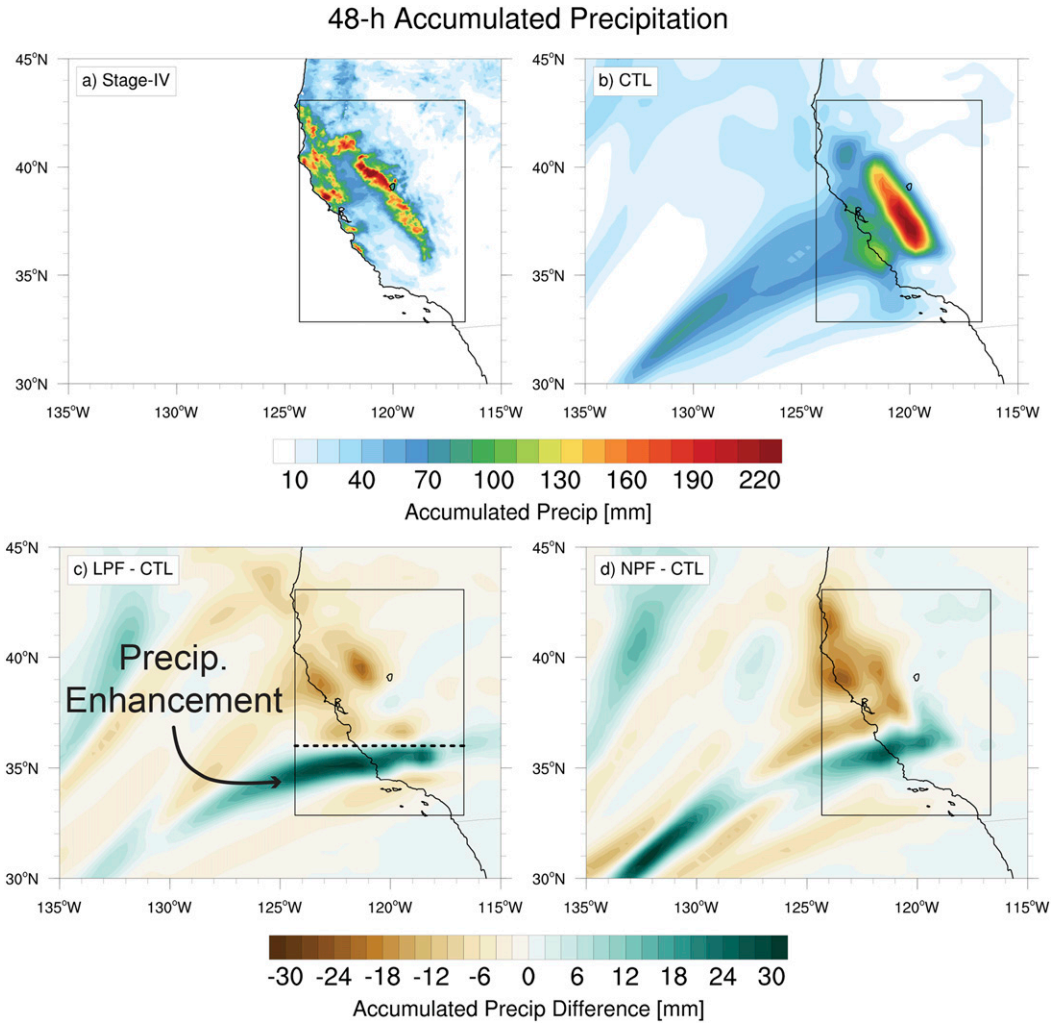

FIG. 2. Plot of the (a) Stage-IV and (b) CTL 48-h accumulated precipitation (mm), and (c) linear perturbations (LPF minus CTL) and (d) nonlinear perturbations (NPF minus CTL) 48-h accumulated precipitation difference fields. The response function box is shown in the solid black box. The thick horizontal dotted black line across the response function box in (c) separates the precipitation enhancement and reduction regions used in Fig. 4 within the box. The precipitation enhancement is identified in (c).

Sierra Nevada range (37°N, 120°W) and central coast, there are some clear biases in the Shasta (42°N, 124°W) and north coastal regions, which results in only a modestly skillful precipitation forecast (Figs. 2a,b). The COAMPS forecast likely does not capture the detailed structure of the observed precipitation at this resolution in part because finescale orographic features, such as the coastal ranges, are not well resolved. Despite these biases, the analysis undertaken here are still valid as they are focused on understanding the physical mechanisms that lead to changes in the forecast. Modest values of precipitation are evident in central California around Morro Bay and San Luis Obispo in both the Stage-IV and the CTL run (Figs. 2a,b). As will be discussed in the next section, this is the region where the most substantial precipitation enhancements occur in the perturbed run.

b. *Initial-condition perturbations*

The COAMPS moist adjoint model provides an objective method for determining sensitivities of the response function (18-h accumulated precipitation averaged within the box shown in Fig. 2) to the initial-condition state variables. Informally speaking, this means that the output of the adjoint model produces the amount by which the 18-h accumulated precipitation will change for a given perturbation in a state variable made at the initial time. As described in section 2a, the perturbations that are employed provide the largest change to the 18-h accumulated precipitation

TABLE 1. The descriptions of acronyms used in this study.

Acronym	Description
CTL	Control nonlinear forecast
LPF	Linear perturbed forecast: the sum of the control nonlinear forecast and the optimal perturbation evolved using the tangent linear model
NPF	Nonlinear perturbed forecast: the nonlinear forecast run from an analysis that is the control analysis plus the initial optimal perturbation
LPF − CTL	Linear perturbation: the optimal perturbation evolved using the tangent linear model, equivalent to the difference between LPF and CTL
NPF − CTL	Nonlinear perturbation: the difference between NPF and CTL

possible within the limit of observational uncertainty and are thereby referred to as the optimal perturbations. These optimal perturbations may be conceptualized as patterns highlighting the regions where the forecast is most sensitive to changes in the initial state. For clarity, the various simulations' acronyms used within this study are shown in Table 1. The nonlinear control simulation is simply CTL; the perturbed tangent linear model's forecast is LPF with difference from the control termed LPF − CTL; and, last, the perturbed nonlinear simulation's forecast is NPF with difference from the CTL termed NPF − CTL.

The initial-condition (0 h) LPF − CTL are shown in Fig. 3 with the CTL run in color fill and the LPF − CTL in the black contours such that solid contours overlaid on positive CTL values indicate an enhancement of the LPF values relative to the CTL. As seen in Figs. 3a and 3b, the 850-hPa optimal perturbations of wind speed and moisture content are situated within and surrounding the tropical moisture plume, or AR, between 130° and 140°W. The 850-hPa moisture is enhanced by up to $0.4\,g\,kg^{-1}$ within a large fraction of the AR core, around 23°N, 140°W, and decreased on the southeast edge, around 20°N, 130°W (Fig. 3b). The 850-hPa wind speed optimal perturbations are seen to increase the wind speed on the tail of the AR (~23°N, 140°W) and near the southeastern edge (~20°N, 130°W); maximum values of these perturbations are up to about $0.15\,m\,s^{-1}$. The optimal perturbations at the 500-hPa level are situated much farther upstream of the AR compared to the lower levels and are located near a jet entrance region (Figs. 3c,d). The fact that the perturbations occur farther upstream with increasing altitude is consistent with the advective speed being much greater at upper levels; if these perturbations are to impact the forecast during the same time period as the lower levels, they must be situated farther away. This is also consistent with the structure of the sensitivities being tilted against the shear (Doyle et al. 2014, 2019; Reynolds et al. 2019) and can be interpreted as growing through potential vorticity (PV) unshielding, which is the result of a superposition of PV maxima, as in the Orr mechanism (Orr 1907; Badger and Hoskins 2001; Reynolds et al. 2001).

4. Results

a. *Evolved perturbations*

The remainder of the manuscript will be focused on the evolution of the optimal perturbations and the dynamical differences between the CTL and the LPF. The difference in 48-h accumulated precipitation between CTL and LPF is shown in Fig. 2c and exhibits a long narrow band of enhanced precipitation centered at the latitude of central California (~35°N) and a modest reduction in precipitation poleward of 36°N. The dipole structure of the precipitation band suggests a shift in the LPF's AR position, however, as will be demonstrated later in this section, the first-order change is in the AR's strength. The fact that the band of enhanced precipitation extends far offshore, away from any topographic features, indicates that it is driven in part by a dynamical mechanism. Similarly, the enhancement over land may be suggestive of orographic effects on precipitation seen at both the coastal mountain ranges of San Luis Obispo (35°N, 121°W) and the southern Sierra Nevada (35.5°N, 119°W). The optimal perturbations are formulated to increase precipitation in the LPF compared to the CTL during the last 18 h of the 48-h forecast. The LPF − CTL domain-averaged 18-h accumulated precipitation is about 3 mm, which is evident when comparing the deeper blue colors to the lighter brown in Fig. 2c. Though this may seem small, it is important to emphasize that this is the overall regional average that is offset by some areas of reduced precipitation.

While the perturbations have been tailored to optimize the precipitation in a linear context, the nonlinear growth of the perturbations may also be examined by making a nonlinear forecast from the optimally perturbed initial state. It is important to compare the forecast of the LPF with the NPF because substantial differences between the two runs may indicate the dominance of nonlinearities, which are not represented within the LPF. The 48-h accumulated precipitation of

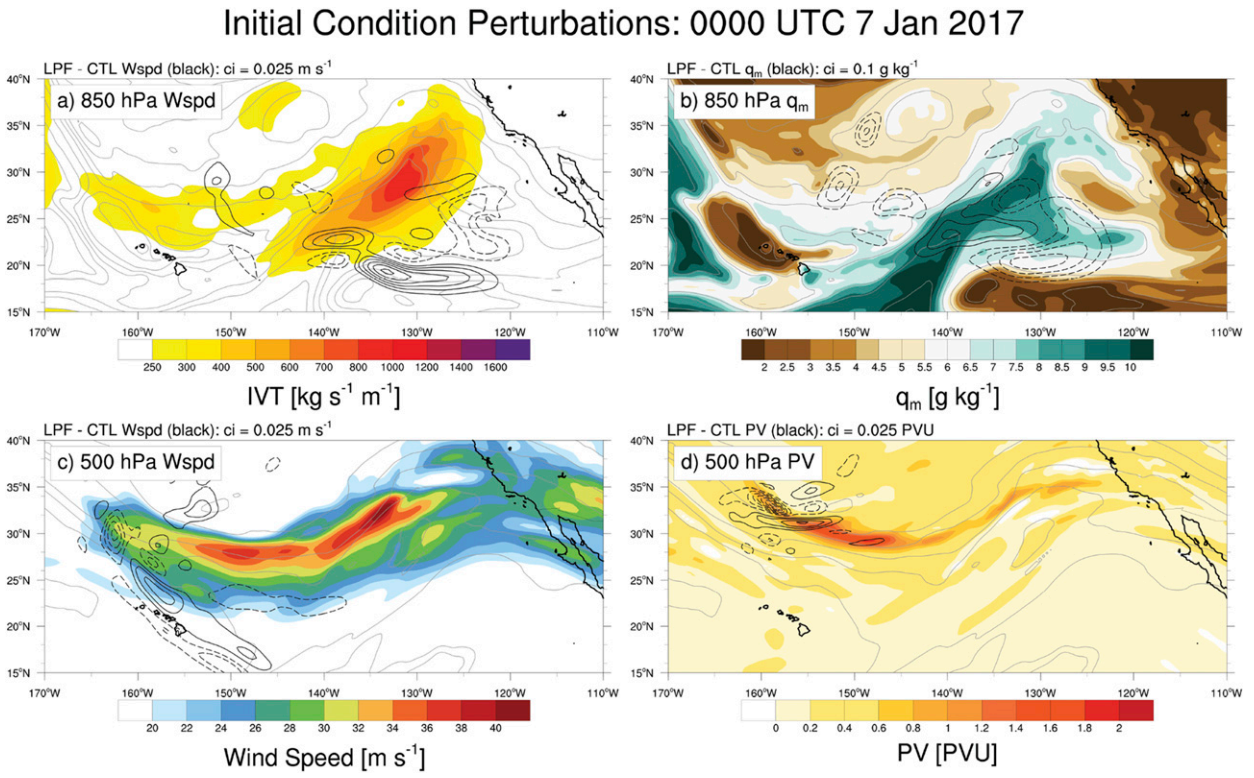

FIG. 3. The initial-condition perturbations for the (a) 850-hPa wind speed with IVT contours (kg s^{-1} m^{-1}; shaded), (b) 850-hPa mixing ratio, (g kg^{-1}; shaded), (c) 500-hPa wind speed (m s^{-1}; shaded), and (d) 500-hPa PV with the LPF − CTL in solid black (positive) and dashed black (negative) contours for each respective field. The solid gray contours in each plot are the equivalent potential temperatures on the respective levels with contour interval (ci) = 4 K and five passes of a five-point local smoother applied.

the NPF − CTL is shown in Fig. 2d. A comparison of the difference fields (Figs. 2c,d) shows that they are qualitatively similar, indicating that within the 48-h forecast, the nonlinearities are sufficiently small such that the linear and nonlinear precipitation perturbations are similar. Therefore, we are confident in moving forward with analyzing the LPF in more detail.

To perform a diagnostic analysis on the differences between the CTL and LPF runs, it is necessary to clarify when in time the evolved perturbations may be leading to the precipitation enhancement. A time series is shown in Fig. 4 of the average accumulated precipitation at 15-min intervals in a region that isolates the precipitation enhancement between the bottom of the response function box up to 36°N indicated by the bold black dotted line in Fig. 2c. The LPF's enhanced precipitation period begins at 26 h, 4 h prior to the response function accumulation period. This is followed by strong growth in the precipitation enhancement that occurs for about 10 h from 26 to 36 h, after which time both the CTL and LPF continue to accumulate precipitation at about the same rate.

The same method of averaging is applied to the IVT field to quantify the role of the orographic precipitation forcing (i.e., moisture transport; Neiman et al. 2016; Martin et al. 2019) within the LPF's enhanced precipitation field (Fig. 4). As can be seen here, elevated values of the LPF's IVT begin at about 24 h, just prior to the start of the period of enhanced precipitation, and end at the same time (36 h). Furthermore, it should be noted that while the percentage increase in IVT in Fig. 4 may seem modest, a map of the difference in IVT between the LPF and CTL (not shown) has a complex pattern of positive and negative values, suggesting that IVT can be

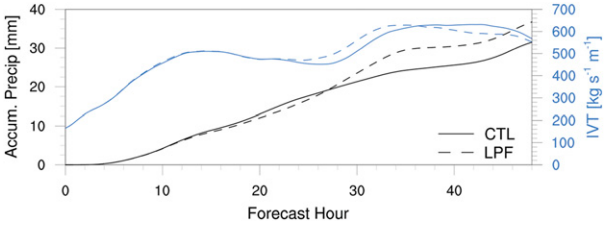

FIG. 4. Time series of average accumulated precipitation (black) and the IVT (blue) within the subregion of Fig. 2c (see text). The control (CTL) run is shown in the solid lines and the linearly perturbed (LPF) run in dashed lines.

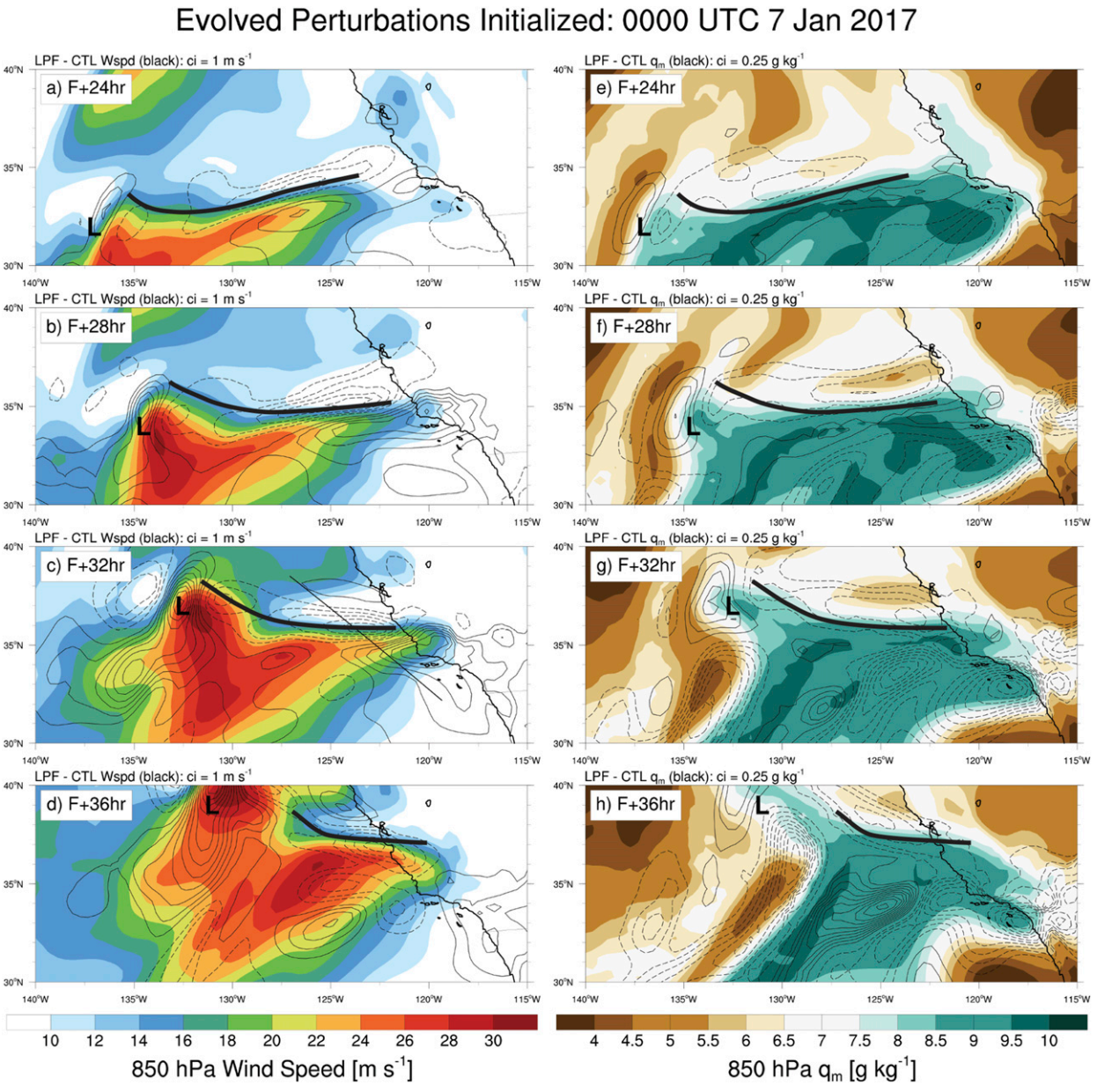

FIG. 5. Plan view every 4 h beginning from 24 h of the 850-hPa (a)–(d) wind speed (m s^{-1}; shaded) and (e)–(h) water vapor mixing ratio (g kg^{-1}; shaded). The LPF − CTL fields are shown in black with solid being positive and dashed being negative values. The approximate position of the low pressure center of the developing secondary cyclone is labeled "L" and the warm front indicated by the thick black curved line. The position of a transect used in Figs. 7–9 is shown in (c) by the thin black straight line.

more locally enhanced than what is reflected in the regional average. Since moisture transport has been shown to correlate well with orographic precipitation (Neiman et al. 2002, 2009; Ralph et al. 2013), this increase in IVT supports the hypothesis that the observed precipitation enhancement is partially due to the increased orographic precipitation forcing.

To further investigate the forcing for orographic precipitation, we examine the components of low-level water vapor transport within the 10-h time period of precipitation enhancement in more detail. From 24 through 36 h, a warm front propagates ahead of the AR (Figs. 5e–h). In this same area as the moisture plume, strong low-level wind speeds directed from the SSW are evident in the CTL run (Figs. 5a–d), indicating a region of very large moisture transport. At 24 h (Figs. 5a,e), 2 h before the enhanced precipitation time period, a strengthening is observed in both the 850-hPa LPF − CTL wind and

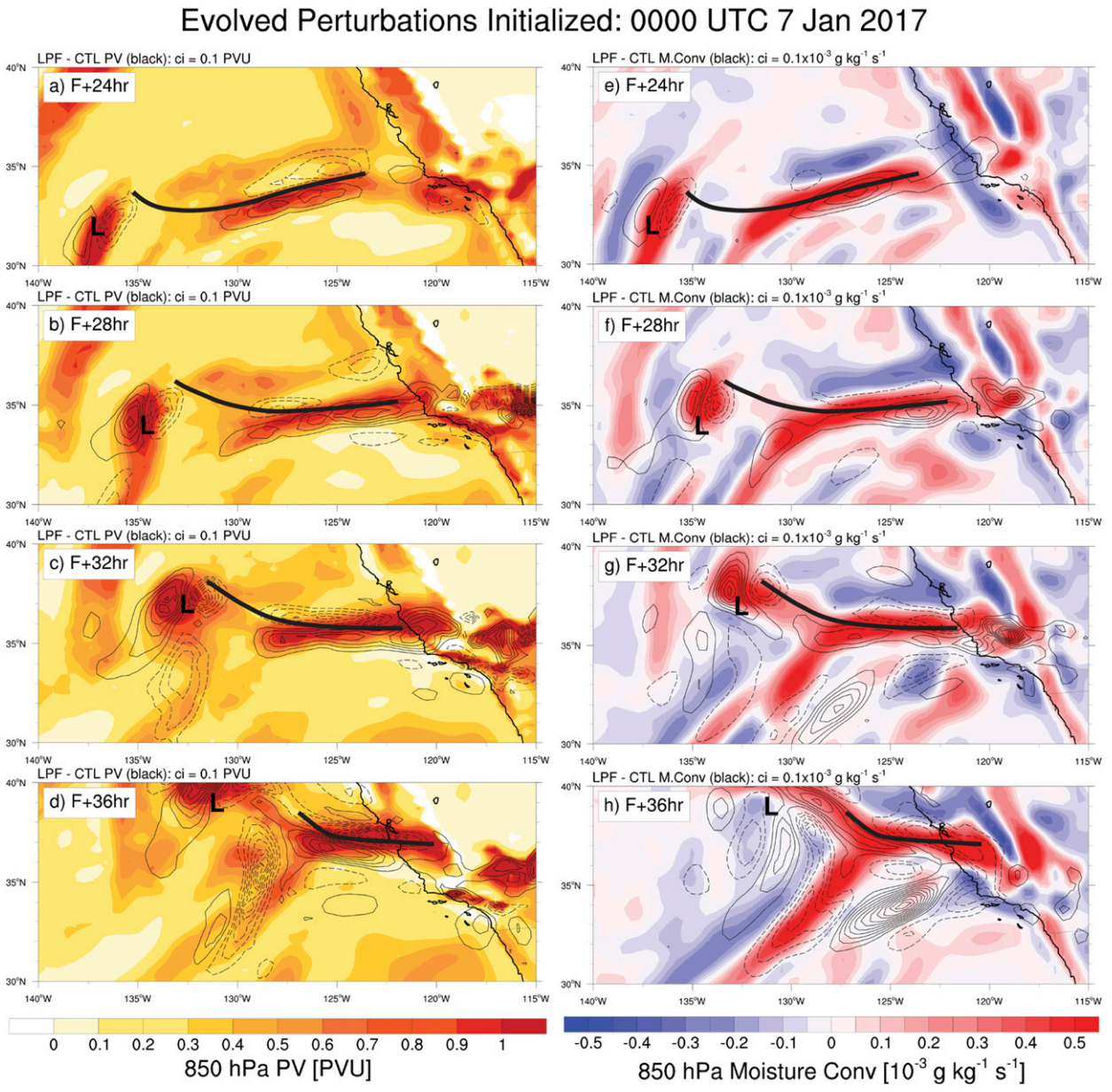

FIG. 6. Plan view every 4 h beginning from 24 h of the 850-hPa (a)–(d) PV (PVU; 1 PVU = 10^{-6} K kg^{-1} m^2 s^{-1}; shaded) and (e)–(h) moisture convergence (10^{-3} g kg^{-1} s^{-1}; shaded; positive is converging). The LPF − CTL fields are shown in black with solid being positive and dashed being negative values. The approximate position of the low pressure center of the developing secondary cyclone is labeled "L" and the warm front is indicated by the thick black curved line. The position of a transect used in Figs. 7–9 is shown in (c) by the thin black straight line.

moisture content behind the warm front. Over the course of the next 8 h, through 32 h, the LPF − CTL wind speed enhancement intensifies substantially while simultaneously propagating northeastward and making landfall (Figs. 5b,c). At 28 h, the moisture enhancement intensifies while remaining coincident with the region of enhanced wind speed (Fig. 5f). By 32 h (Fig. 5g), the moisture is no longer enhanced behind the warm front, likely a result of the greater precipitation taking place. Finally, at 36 h (Figs. 5d,h) both the LPF − CTL wind and moisture content are reduced behind the warm front. As mentioned previously, the increase in vapor transport supports the hypothesis that the precipitation enhancement is partially due to a greater orographic precipitation forcing.

During this same time period, from 24 through 36 h, an intensifying narrow band of moisture convergence ($-q_m\nabla \cdot \mathbf{u}$) and low-level PV is situated behind the warm front in the CTL (Fig. 6). At 24 h (Figs. 6a,e), there

is already substantially enhanced moisture convergence behind the warm front in the LPF − CTL, which results in diabatic generation of PV. Over the next 8 h, both the moisture convergence and PV are enhanced in LPF − CTL while the system is making landfall (Figs. 6b–c, f–g). Since the CTL fields are also intensifying during this time period, the fact that the LPF − CTL field is enhanced at these times shows that the rate of intensification for these quantities is greater in the LPF than the CTL. By 36 h, the coherent moisture convergence dipole structure off the CA coast in the LPF − CTL is less apparent while the PV dipole appears relatively unchanged (Figs. 6d,h). Just as Fig. 5 indicates that the forcing for orographic precipitation is enhanced within the LPF, Fig. 6 shows that dynamically driven precipitation is enhanced through moisture convergence.

To provide analysis of the vertical structure, Fig. 7 shows a cross section taken across the warm front (location shown in Fig. 5c) at the start of the response function integration time (forecast hour 30) in which the precipitation enhancement is occurring. At this time, the CTL exhibits strong wind speeds of up to 25 m s^{-1} at 900 hPa situated on the southeast side of the low-level PV anomaly centered on the front (Figs. 7a,b). A dipole structure is observed in the LPF − CTL low-level wind speed (Fig. 7a), where enhancements of up to 6 m s^{-1} indicate the clear development of a low-level jet at 900 hPa that was not present in the CTL simulation. At first glance, this may seem to be a shift in the wind speed locations, but examination of the total LPF wind fields (not shown) compared with that of the CTL clearly shows the winds are enhanced up to 20% rather than shifted. In fact, the location of this dipole is centered on the PV enhancement (Fig. 7b), which matches the expected horizontal circulation change due to low-level latent heating as investigated by Lackmann (2002). Importantly, the mixing ratio enhancements (Fig. 7d) are found to overlap the region of strengthened wind speed, consistent with the observed enhancement of IVT. The reason that the region of enhanced vapor transport is not directly coincident with the enhanced precipitation in this cross section is because the section location is well offshore where orographic influences are not present.

Strong vertical motion that is vertically sloped and oriented along equivalent potential surfaces occurs in the CTL (not shown) and also approximately along the region of moisture convergence (Figs. 7c,e). Examination of equivalent potential temperature and absolute momentum (not shown) clearly indicate that this sloped region is symmetrically unstable, demonstrating that perturbations are expected to grow rapidly there. Contrastingly, the LPF − CTL vertical motion clearly has two distinct regions, one with a slantwise orientation, similar to that of the CTL, and the other with a distinct vertical orientation (Figs. 7c,e) consistent with deep convection as in Cordeira et al. (2013). Cross sections of convective available potential energy (CAPE; not shown) indicate that the LPF has an environment that is more conducive to convection. A greater degree of convection is likely also a component of the precipitation enhancement, although this is not investigated further here, and thus remains an open question for future work. As demonstrated by the clear increase in both the vertical ascent and vapor transport, the cross sections further support the hypothesis that the observed precipitation enhancement is a result of contributions from the dynamic precipitation component and orographic precipitation forcing.

b. *The transverse circulation*

The Sawyer–Eliassen transverse circulation model, which produces the vertical and cross-frontal ageostrophic circulation perpendicular to the upper-level jet structure in an approximately straight flow, is used to further investigate the dynamical component of the precipitation enhancement by separating the vertical velocity and moisture convergence into moist and dry components. Here, the moist processes are due to the latent heating effects while the dry forcing components arise from quasigeostrophic shearing and stretching deformation contributions [see Keyser and Shapiro (1986) and Winters and Martin (2014) for a more in-depth description]. The dry and moist components are obtained by solving the equation in a piecewise manner by using the dry and moist forcings individually within the PDE solver. Note that Figs. 8 and 9 show only a subset of the full PDE solver's domain to match the previous cross sections in Fig. 7.

While the Sawyer–Eliassen model directly yields the components of the transverse circulation (v_{ag}, ω), we investigate the moisture convergence rather than v_{ag} because it is more relevant for explaining the precipitation enhancement. The Sawyer–Eliassen-derived moisture convergence is calculated in three steps: 1) solve the Sawyer–Eliassen equation for the ageostrophic streamfunction (Ψ), 2) calculate the cross-jet ageostrophic wind using the equation $v_{ag} = -(\partial\psi/\partial p)$, and 3) assume 2D convergence in the plane of the cross section such that $\mathrm{MConv} = -q_m(\partial v_{ag}/\partial y)$, where y is the cross-jet streak direction. The Sawyer–Eliassen-derived total moisture convergence (Fig. 8a) is calculated along the same transect as Fig. 7, and compares very well with the full 3D model calculated moisture convergence in regard to strength, slope, and vertical extent (Fig. 7e). Similarly, the Sawyer–Eliassen model reproduces the LPF − CTL moisture convergence very closely in terms

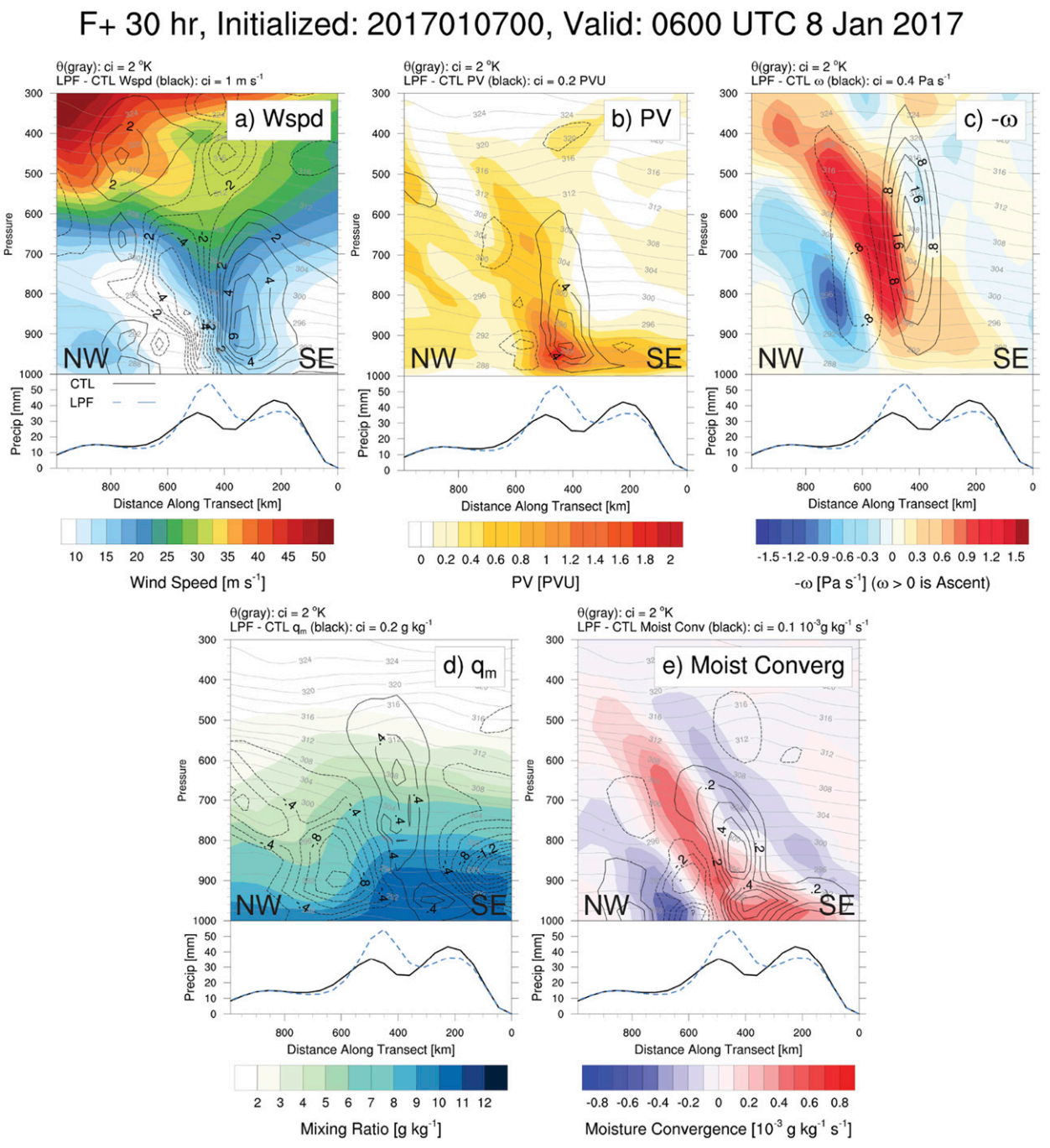

FIG. 7. Cross sections at 30 h along the transect shown in Fig. 5c with "NW" being the northwest side and "SE" being the southeast side of (a) wind speed ($m\,s^{-1}$; shaded), (b) PV (PVU; shaded), (c) negative omega ($Pa\,s^{-1}$; shaded), (d) mixing ratio ($g\,kg^{-1}$; shaded), and (e) moisture convergence ($10^{-3}\,g\,kg^{-1}\,s^{-1}$; shaded). The LPF − CTL fields are shown in black with solid being positive and dashed being negative values. The bottom plot in each panel (below each transect) shows the accumulated precipitation for the CTL (solid black) and the LPF (dashed blue).

of strength, slope, and vertical extent (solid black contours), though it has a maximum at the surface (Fig. 8a), while the real case (Fig. 7e) is slightly elevated from the surface. Therefore, despite the assumptions included in the Sawyer–Eliassen equation, it still provides a very accurate depiction of the transverse circulation in this case.

The main utility of the Sawyer–Eliassen model for this analysis is the ability to separate the transverse

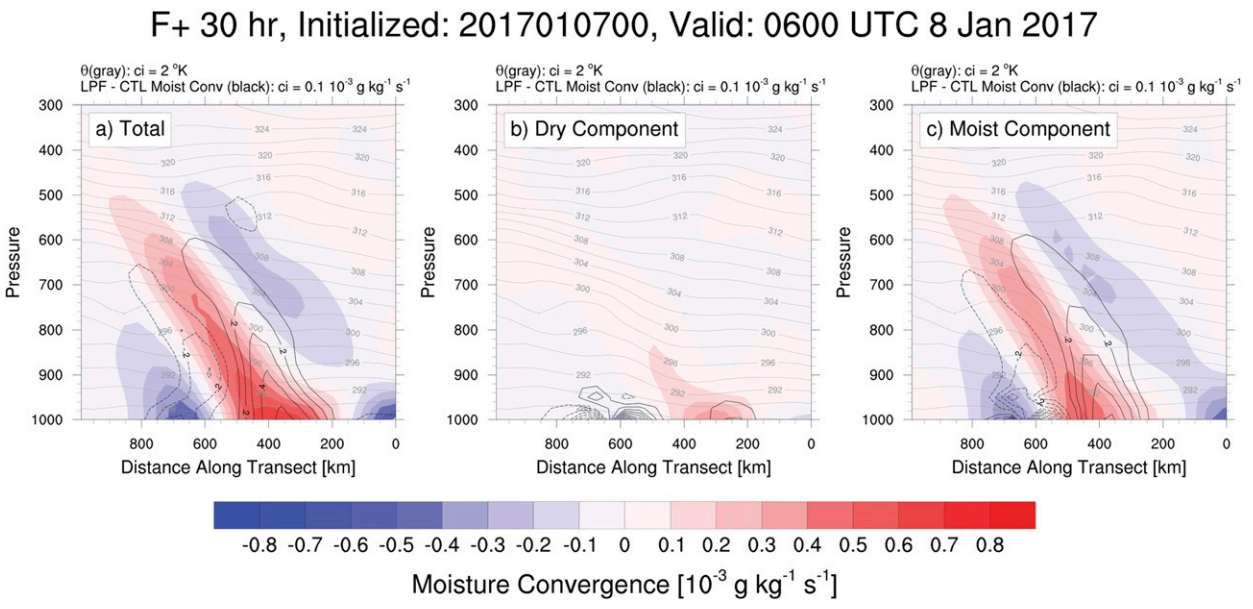

FIG. 8. Cross sections at 30 h along the transect shown in Fig. 1i of the Sawyer–Eliassen-derived moisture convergence (10^{-3} g kg^{-1} s^{-1}; shaded) for the (a) total, (b) quasigeostrophic (dry) component, and (c) diabatic (moist) component. The LPF − CTL fields are shown in black with solid being positive and dashed being negative values.

circulation into the dry and moist components. The geostrophic (dry) and the diabatic (moist) components of moisture convergence shown in Figs. 8b and 8c, respectively, clearly illustrate that the moist component is dominant. The dry component is constrained to the very lowest levels (Fig. 8b) with peak values being much smaller than those observed (Fig. 7e). Conversely, the moist component has peak values, slope, and vertical extent that are much closer to that of the CTL (Fig. 8c). With that said, the dry component is not negligible. Furthermore, it is important to be cognizant that this analysis is only at a single time, which raises the question

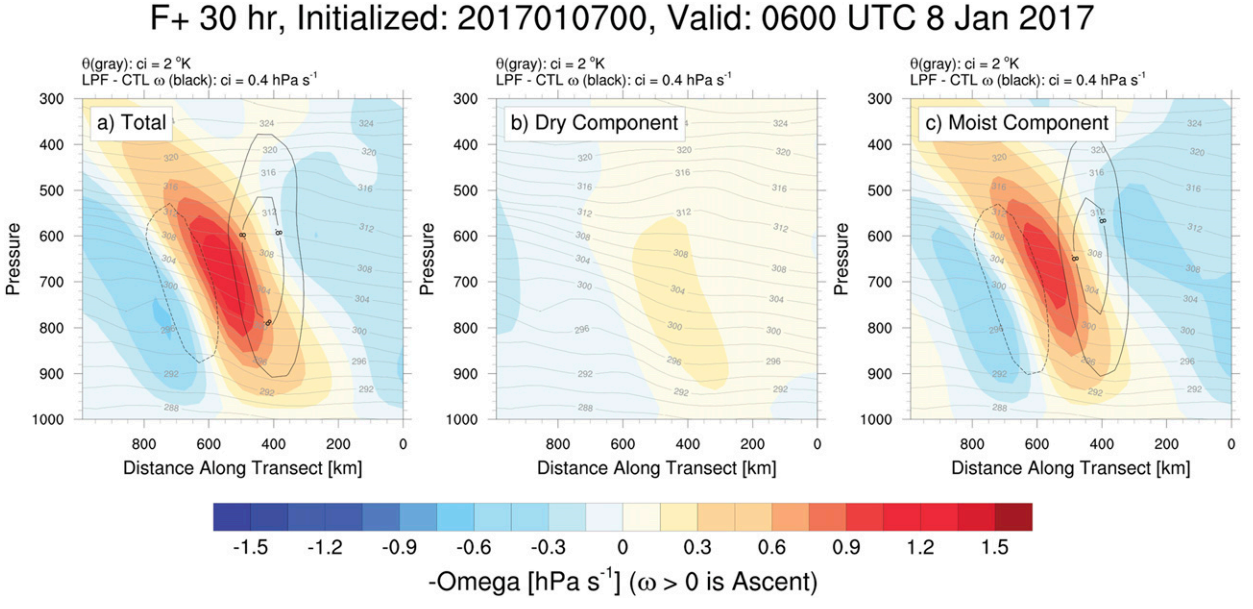

FIG. 9. Cross sections at 30 h along the transect shown in Fig. 1i of the Sawyer–Eliassen-derived vertical velocity (10^{-3} g kg^{-1} s^{-1}; shaded) for the (a) total, (b) quasigeostrophic (dry) component, and (c) diabatic (moist) component. The LPF − CTL fields are shown in black with solid being positive and dashed being negative values.

of what role the dry component had at an earlier time. Did the dry component have much greater strength earlier on? Did the LPF − CTL dry component at an earlier time initiate the LPF − CTL moist component? These questions will be addressed in section 4c.

Vertical velocity can also be calculated from the Sawyer–Eliassen analysis by using $\omega = \partial\psi/\partial y$ (Fig. 9). Comparison of the total Sawyer–Eliassen-derived vertical velocity (Fig. 9a) to that of the 3D model output (Fig. 7c) indicates it is also accurate, though not to the degree of the moisture convergence comparisons. The CTL vertical velocity derived by the Sawyer–Eliassen method retains the sloped orientation and vertical extent but is biased low in magnitude. This is attributed to the fact that it is a modestly convective region as indicated by the CAPE values ($\sim$300 J kg^{-1}; not shown), which is not accounted for by the Sawyer–Eliassen analysis. Similarly, while the slope and vertical extent of LPF perturbation vertical velocities are reproduced well, there is a low bias in magnitude. It is important to note that the vertically upright orientation of LPF perturbations (Fig. 9a) is reproduced very well in the Sawyer–Eliassen model implying that it is not only due to convection but also a result of the forced ascent. As in the results for moisture convergence, the vertical velocity is dominated by the moist component term at this time.

c. *Pseudo-Lagrangian evolution of the transverse circulation*

The transverse circulation analysis above applies only to one cross section at a single time, so a complimentary analysis is undertaken by initializing backward trajectories from the central point along the cross section of Figs. 7–9 to investigate a system-relative evolution of the transverse circulation. At each point along each trajectory in Fig. 10a, a cross section is drawn to be nearly perpendicular to the upper-level jet streak (not shown). This establishes a pseudo-Lagrangian cross-sectional time series for each trajectory. It is important to note that it is called ''pseudo-Lagrangian'' because it assumes that the entire cross section moves together, which, of course, is not the case. Despite this caveat, animations of the cross sections along the pseudo-Lagrangian trajectory produce what seem to be an accurate depiction of how the system-relative cross section evolves (not shown). While the pseudo-Lagrangian cross-section time series can address whether the results in section 4b are applicable for other times, it does not address the spatial issue. A simple way to investigate how the results from section 4b may vary spatially is to initiate the backward trajectory at the same point as in Fig. 10a, but at different times. Since the system is moving, this will ensure that different portions of the AR are sampled. This was done for backward trajectories initiated at 24 through 36 h with each air parcel moving all the way backward to the initial time at 0 h (Fig. 10a). This method produces 13 pseudo-Lagrangian cross-section time series each for CTL and LPF from which the following analysis is derived.

The strength of the Sawyer–Eliassen transverse circulation for each component is measured from the maximum value of $-\omega$ for each time step along the pseudo-Lagrangian cross section. This is repeated for each of the 13 pseudo-Lagrangian trajectories, and then averaged by aligning them on the respective final trajectory times (Fig. 10b). Consistent with previous results, the strength of the LPF − CTL vertical velocity is found to be substantially greater than that of the CTL. Furthermore, the moist component is dominant from about 10 h onward in both the CTL and LPF; the dry component remains very steady from beginning to end. This analysis shows that dominance of the moist component of the transverse circulation applies not only to a single transect at a single time, but consistently influences the dynamics of the transverse circulation for the system as a whole.

A major benefit of creating a time series of the transverse circulation strength is that it allows us to form conclusions about its evolution. It reveals that the LPF's vertical velocity enhancement is initiated from the moist component starting at about 12 h (Fig. 10b), at which time the slope of the LPF curve becomes greater than the CTL. Sustained LPF vertical velocity growth continues up until about 26 h at which point the CTL remains steady, and the LPF begins to decline in strength. The CTL and LPF total vertical velocities are clearly controlled by their respective moist components with the dry components providing a small, but steady contribution. Both the CTL and LPF have very similar dry component strengths, indicating that the quasi-geostrophic shearing and stretching environments are approximately the same between the different runs.

The decomposition of the moist and dry forcings in the Sawyer–Eliassen transverse circulation analysis suggests the possibility of a positive feedback mechanism. Latent heating at the developing frontal boundary provides a positive forcing to the Sawyer–Eliassen circulation. This positive forcing in turn leads to moisture convergence, which may then drive further latent heat release. While it is outside of the scope of this study to prove that this is indeed a feedback mechanism, it is still clear that the dynamical component of the vertical velocity is highly dependent on the nature of the moist processes and, thereby, on the moisture content.

d. *Lagrangian evolution of the optimal perturbations*

Until this point, this study has been focused on the evolved perturbations with only some minimal

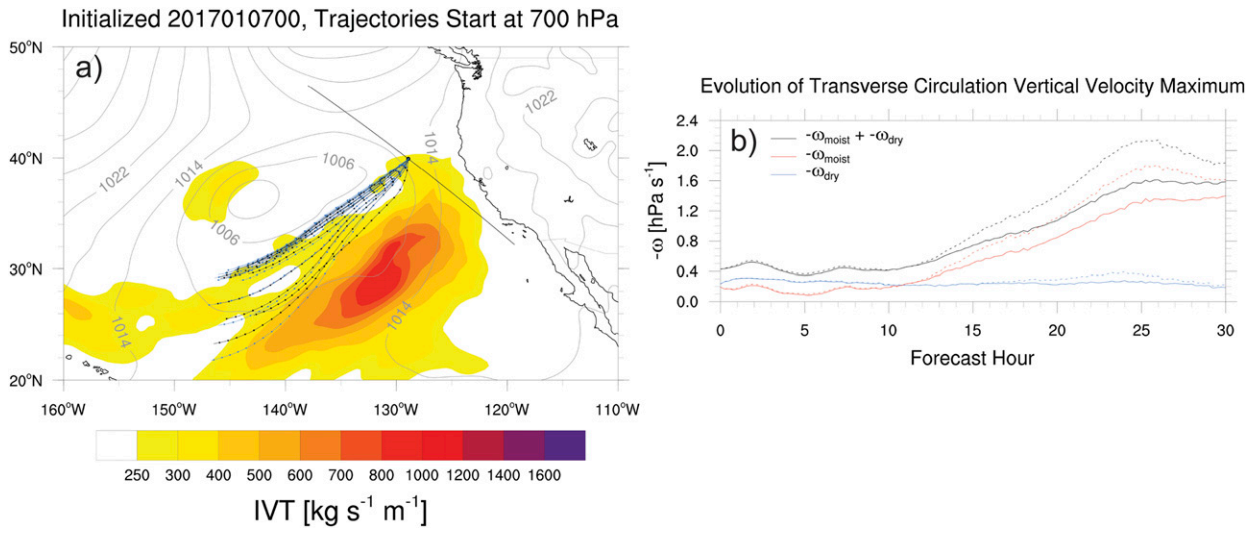

FIG. 10. (a) Plan view of the initial time IVT ($kg\,s^{-1}\,m^{-1}$; color fill) and SLP (contoured every 4 hPa; solid gray) with the backward trajectories of the CTL (black) and LPF (blue). The hourly locations of the air parcels are shown in the filled circle along each trajectory. The final time transect is shown as a reference in the solid black line. The trajectories are initialized at 700 hPa and are separated in time at 1-h intervals starting from 24 to 36 h. (b) The average Sawyer–Eliassen $-\omega$ ($hPa\,s^{-1}$) along the trajectories shown in (a). The total value of $-\omega$ is in black with the moist component in red and the dry component in blue. The CTL is shown in the solid lines with the LPF in the dashed.

connections to the initial optimal perturbations. To address this gap, forward trajectories are utilized to investigate how the optimally perturbed regions may connect to the downstream processes described previously. Forward trajectories are initialized on the 700-hPa level, where the largest moisture perturbations were made, at 0 h in a 11×11 square block with a 40-km spacing and centered on the maximum positive initial-condition moisture perturbation (Fig. 11a). This will enable the initial perturbations to be connected to the moist transverse circulation analysis already discussed. It is clear from Fig. 11a that the LPF trajectories are more tightly clustered than the CTL trajectories, consistent with stronger convergence from the enhanced transverse circulation.

The average Lagrangian (along the air parcel trajectory) moisture content, PV, and pressure are shown in Fig. 11b for the CTL and LPF. To ensure that the shape of the averaged curves is representative of the individuals, each trajectory is shifted in time to match a clear rise in moisture content (Fig. 11b, at 23 h) immediately followed by a sharp decline, which is a feature found to be present among all trajectories. The average time axis among all of the trajectories is used in order to provide a sense of the time scale. The three subplots in Fig. 11b illustrate a three-phase sequence, which is not only very consistent with the previous results pertaining to the transverse circulation, but also ties the sequence of events back to the initial perturbations. At the start of phase I (6–20 h), it is clear that the LPF air parcels have enhanced moisture content, a direct result of the perturbation. As phase I progresses, both the CTL and the LPF moisture content have a very small, but steady increase, with the LPF maintaining greater moisture throughout. No substantial changes occur for PV or pressure during this phase for these trajectories.

Phase II (20–24 h) is short but distinctly indicates that the growth rate of the moisture content in both the LPF and the CTL increases noticeably. During this time, a rise in PV indicates that diabatic generation has begun, with the perturbed LPF exhibiting a substantially greater increase than CTL. Both observations are consistent with the moisture convergence processes previously described, which can cause an increase in moisture content and serve to diabatically generate PV. Throughout phase II, the air parcel pressure remains mostly steady with only a modest decrease in height (increase in pressure).

Last, in phase III (24–30 h), the air parcels begin their rapid ascent in the warm conveyor belt (Wernli and Davies 1997; Wernli 1997; Schemm et al. 2013), which is also confirmed from the plan-view sequence shown in Fig. S1 in the online supplemental material. The PV reaches a maximum, and the moisture content rapidly decreases, likely due to precipitation. During the first few hours of phase III, the LPF ascent rate is initially much greater than that of the CTL and, in turn, it

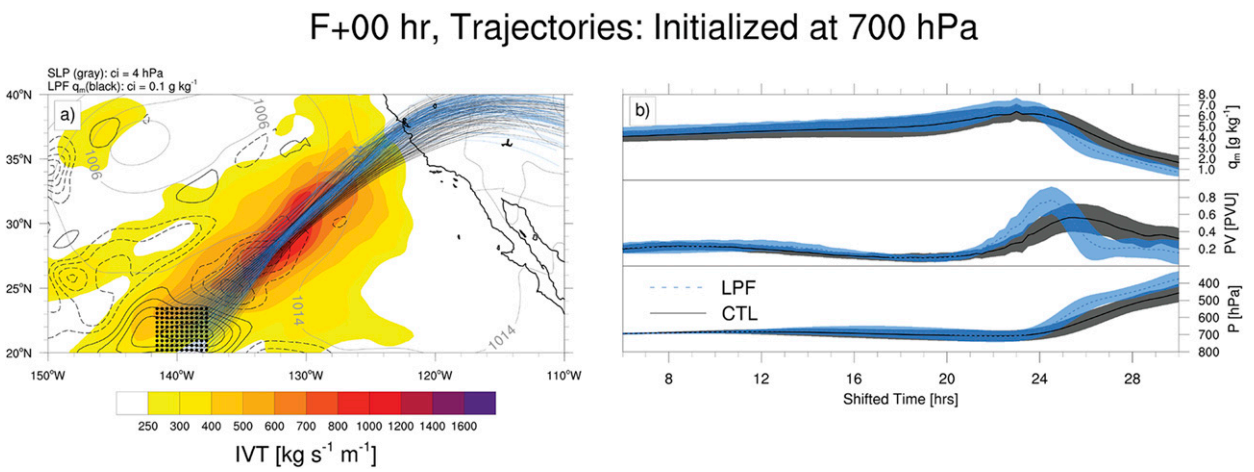

FIG. 11. (a) A plan view of the initial time IVT (kg s^{-1} m^{-1}; color fill), SLP (contoured every 4 hPa; solid gray), and initial-condition LPF-CTL (black contours with solid being positive and dashed being negative values). Forward trajectories are shown for CTL (black) and LPF (blue) with the initialization points shown in black filled circles. (b) (top) Mixing ratio (g kg^{-1}), (middle) PV (PVU), and (bottom) pressure (hPa) following the air parcel trajectories shown in (a) for the CTL (solid black) and LPF (dashed blue). The average of all trajectories is shown in bold with one standard deviation from the mean shown in the transparent color fill. The trajectories in (b) are shifted in time to center each trajectory on the same feature (described in text).

reaches a higher overall elevation by 30 h. The LPF's enhanced ascent rate and PV is consistent with the analysis of the transverse circulation in sections 4b and 4c in that stronger moist processes lead to greater ascent. This coherence suggests that the physical process leading to the observed Lagrangian evolution in Fig. 11b are actually those described by the transverse circulation.

A similar analysis is performed by initializing another 11 × 11 box of air parcels centered on the negative moisture perturbation at approximately 26.5°5N, 135.5°5W. The parcel trajectories (not shown) terminate in Southern California and Northern Baja, Mexico (32°N, 117°W), which is outside of the response function domain. Therefore, the Lagrangian approach to understanding the mechanism for increasing precipitation is not applicable to this region, and the impact on precipitation from these perturbations must be coming from changes to the evolving dynamics not captured in a Lagrangian framework. For example, it may be that the negative perturbations are associated with changes to the initial cyclone (AR wave 1) and not the frontal wave (AR wave 2).

The consistency between the Lagrangian evolution of the optimal moisture perturbation with the enhancements observed in the transverse circulation provides a connection between the initial perturbations and their downstream modifications of important physical processes. The forward trajectory analysis supports the hypothesis that the positive moist optimal perturbations are positioned, at least in part, to provide more moisture available for enhanced latent heat release. Enhanced latent heating leads to an increase in the dynamical component of the precipitation through the enhanced transverse circulation. This analysis demonstrates the utility of the Lagrangian air parcel trajectory method in tracking the evolution of the optimal perturbations. While outside the scope of this work, a future study could initialize air parcels in this way for different areas within all the largest initial-condition perturbation areas and track their evolution.

5. Conclusions and discussion

This study is focused on understanding the nature of rapid perturbation growth in a tangent linear model for an extreme landfalling AR. The perturbed tangent linear forecast (LPF) has been optimized following Doyle et al. (2019) to enhance the final 18 h of the accumulated precipitation in an area of California and within the constraints of analysis uncertainty. In agreement with Cannon et al. (2018), the analysis presented here demonstrates that the precipitation enhancement in the perturbed run is a result of both the enhanced orographic precipitation forcing and the dynamic precipitation component. Importantly, evidence suggests that the enhancement of both components originate from the same latent heating process, thereby making the precipitation forecast particularly sensitive to errors in initial-condition moisture content.

The sequence of events in which the moisture perturbations enhance precipitation is illustrated schematically in

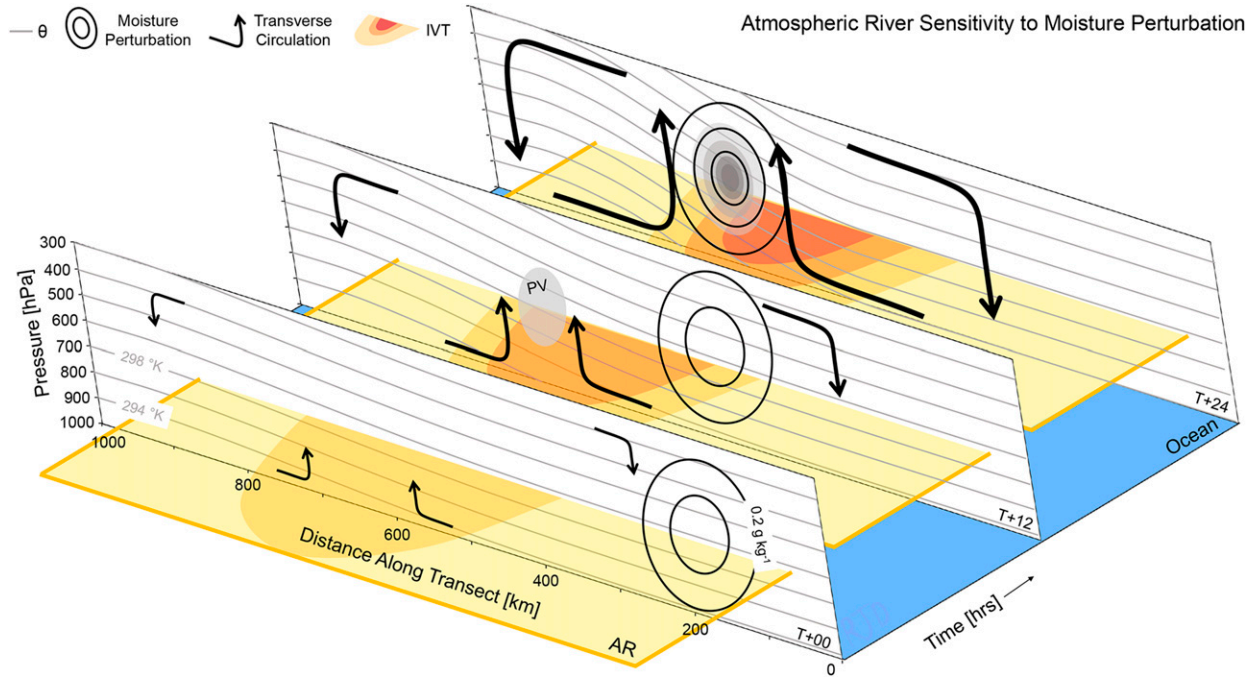

FIG. 12. A pseudo-4D schematic illustrating the evolution of cross sections in an AR-relative reference frame. The IVT values of the AR are shown using the yellow to red shading (small to large values, respectively). The cross sections show potential temperature as gray contours, the LPF moisture perturbation as black contours, and the transverse circulation in the plane of the cross section as the black arrows with the strength indicated by the length and arrow thickness.

Fig. 12. At $T + 0$ h, the positive moisture perturbation is initiated on the periphery of the AR where it is gradually fed into the developing frontal zone. Starting at $T + 12$ h, PV is diabatically generated at the frontal zone through moisture convergence and the subsequent release of latent heat. The wind field responds to the PV anomaly by increasing (decreasing) on the warm (cool) side of the front following Lackmann (2002), thereby leading to a local enhancement of moisture transport. The transverse circulation responds to the latent heat release by strengthening the moisture convergence and ascent at the frontal zone. During this development, the moisture perturbation remains mostly unchanged and continues its way toward the front. Finally, at $T + 24$ h, the moisture perturbation reaches the frontal zone leading to substantial latent heat enhancements. This additional heating enhancement, along with the sustained latent heating independent of the perturbation, drives an even greater moisture transport through the generation of a stronger PV anomaly, and an amplification in the transverse circulation as described by the Sawyer–Eliassen model.

The observation that the initial moisture perturbation is fed into the region of moisture convergence aligns well with the results of Reynolds et al. (2019) and Doyle et al. (2014, 2019). They found that the optimal perturbations within ARs exhibit upshear tilts that can extract energy from the mean flow through the PV unshielding mechanism. The results presented here are consistent with the hypothesis that the physical "reason" why the moist adjoint sensitivity adds moisture within the AR for this case is so that it may serve to enhance latent heating processes and thereby enhance both the orographic and dynamic components of the precipitation.

Clearly, moist processes are critically important in the development of the strong transverse circulation, which is itself responsible for the strong moisture convergence and latent heating. Since the Sawyer–Eliassen model is also forced by a latent heating term, these results suggest a feedback mechanism whereby the latent heating is both a source and a consequence of the transverse circulation. This may be important from a predictability standpoint because it demonstrates a mechanism by which small changes in the initial moisture content can lead to large changes in the forecast downstream. For example, targeted observational campaigns should closely consider sampling in the moist regions that feeds into the transverse circulation since any error in those regions can grow substantially. Furthermore, since the transverse circulation is a frequent component of ECs, and ECs are often accompanied by ARs (Zhang et al. 2019), the results of this case study are likely to be representative of a large number of ARs.

Acknowledgments. This work was supported by the U.S. Army Corps of Engineers from the Award USACE W912HZ-15-2-0019. The authors thank the support of the entire CW3E team for their useful thoughts and comments on this work. In particular we thank Luca Delle Monache, Forest Cannon, Anna Wilson, Julie Kalansky, Caroline Papadopoulos, and Brian Kawzenuk. The lead author acknowledges C.A.R. and J.D.D. and gratefully acknowledges the support of the Chief of Naval Research through the NRL Base Program, precipitation enhancement 0601153N. Computational resources were provided by the Navy DSRC in Stennis, Mississippi.

REFERENCES

Alpert, P., 1986: Mesoscale indexing of the distribution of orographic precipitation over high mountains. *J. Climate Appl. Meteor.*, **25**, 532–545, https://doi.org/10.1175/1520-0450(1986)025<0532:MIOTDO>2.0.CO;2.

Amerault, C., X. Zou, and J. D. Doyle, 2008: Tests of an adjoint mesoscale model with explicit moist physics on the cloud scale. *Mon. Wea. Rev.*, **136**, 2120–2132, https://doi.org/10.1175/2007MWR2259.1.

Badger, J., and B. J. Hoskins, 2001: Simple initial value problems and mechanisms for baroclinic growth. *J. Atmos. Sci.*, **58**, 38–49, https://doi.org/10.1175/1520-0469(2001)058<0038:SIVPAM>2.0.CO;2.

Bjerknes, J., and H. Solberg, 1922: Life cycle of cyclones and the polar front theory of atmospheric circulation. *Geofys. Publ.*, **3**, 1–18.

Bryan, G. H., 2008: On the computation of pseudoadiabatic entropy and equivalent potential temperature. *Mon. Wea. Rev.*, **136**, 5239–5245, https://doi.org/10.1175/2008MWR2593.1.

Cannon, F., C. Hecht, J. Cordeira, and F. M. Ralph, 2018: Synoptic to mesoscale forcing of extreme precipitation in Southern California. *J. Geophys. Res. Atmos.*, **123**, 13 714–13 730, https://doi.org/10.1029/2018JD029045.

Cordeira, J. M., F. M. Ralph, and B. J. Moore, 2013: The development and evolution of two atmospheric rivers in proximity to western North Pacific tropical cyclones in October 2010. *Mon. Wea. Rev.*, **141**, 4234–4255, https://doi.org/10.1175/MWR-D-13-00019.1.

DeFlorio, M., D. Waliser, B. Guan, D. Lavers, F. M. Ralph, and F. Vitart, 2018: Global assessment of atmospheric river prediction skill. *J. Hydrometeor.*, **19**, 409–426, https://doi.org/10.1175/JHM-D-17-0135.1.

Dettinger, M. D., 2013: Atmospheric rivers as drought busters on the U.S. West Coast. *J. Hydrometeor.*, **14**, 1721–1732, https://doi.org/10.1175/JHM-D-13-02.1.

——, and D. Cayan, 2014: Drought and the California delta—A matter of extremes. *San Francisco Estuary Watershed Sci.*, **12**, https://doi.org/10.15447/SFEWS.2014V12ISS2ART4.

Doyle, J. D., C. A. Reynolds, and C. Amerault, 2011: Diagnosing tropical cyclone sensitivity. *Comput. Sci. Eng.*, **13**, 31–39, https://doi.org/10.1109/MCSE.2010.146.

——, ——, ——, and J. Moskaitis, 2012: Adjoint sensitivity and predictability of tropical cyclogenesis. *J. Atmos. Sci.*, **69**, 3535–3557, https://doi.org/10.1175/JAS-D-12-0110.1.

——, C. Amerault, C. A. Reynolds, and P. A. Reinecke, 2014: Initial condition sensitivity and predictability of a severe extratropical cyclone using a moist adjoint. *Mon. Wea. Rev.*, **142**, 320–342, https://doi.org/10.1175/MWR-D-13-00201.1.

——, C. A. Reynolds, and C. Amerault, 2019: Adjoint sensitivity analysis of high-impact extratropical cyclones. *Mon. Wea. Rev.*, **147**, 4511–4532, https://doi.org/10.1175/MWR-D-19-0055.1.

Eliassen, A., 1962: On the vertical circulation in frontal zones. *Geophys. Publ.*, **24**, 147–160.

Emanuel, K. A., M. Fantini, and A. J. Thorpe, 1987: Baroclinic instability in an environment of small stability to slantwise moist convection. Part I: Two-dimensional models. *J. Atmos. Sci.*, **44**, 1559–1573, https://doi.org/10.1175/1520-0469(1987)044<1559:BIIAEO>2.0.CO;2.

Errico, R. M., 1997: What is an adjoint model? *Bull. Amer. Meteor. Soc.*, **78**, 2577–2591, https://doi.org/10.1175/1520-0477(1997)078<2577:WIAAM>2.0.CO;2.

——, and K. D. Raeder, 1999: An examination of the accuracy of the linearization of a mesoscale model with moist physics. *Quart. J. Roy. Meteor. Soc.*, **125**, 169–195, https://doi.org/10.1002/qj.49712555310.

Fish, M. A., A. M. Wilson, and F. M. Ralph, 2019: Atmospheric river families: Definition and associated synoptic conditions. *J. Hydrometeor.*, **20**, 2091–2108, https://doi.org/10.1175/JHM-D-18-0217.1.

Gray, W. M., C. Neumann, and T. L. Tsui, 1991: Assessment of the role of aircraft reconnaissance on tropical cyclone analysis and forecasting. *Bull. Amer. Meteor. Soc.*, **72**, 1867–1884, https://doi.org/10.1175/1520-0477(1991)072<1867:AOTROA>2.0.CO;2.

Hewson, T. D., 2009: Diminutive frontal waves—A link between fronts and cyclones. *J. Atmos. Sci.*, **66**, 116–132, https://doi.org/10.1175/2008JAS2719.1.

Hodur, R. M., 1997: The Naval Research Laboratory's Coupled Ocean/Atmosphere Mesoscale Prediction System (COAMPS). *Mon. Wea. Rev.*, **125**, 1414–1430, https://doi.org/10.1175/1520-0493(1997)125<1414:TNRLSC>2.0.CO;2.

Keyser, D., and M. A. Shapiro, 1986: A review of the structure and dynamics of upper-level frontal zones. *Mon. Wea. Rev.*, **114**, 452–499, https://doi.org/10.1175/1520-0493(1986)114<0452:AROTSA>2.0.CO;2.

Lackmann, G. M., 2002: Cold-frontal potential vorticity maxima, the low-level jet, and moisture transport in extratropical cyclones. *Mon. Wea. Rev.*, **130**, 59–74, https://doi.org/10.1175/1520-0493(2002)130<0059:CFPVMT>2.0.CO;2.

Lamjiri, M. A., M. D. Dettinger, F. M. Ralph, and B. Guan, 2017: Hourly storm characteristics along the U.S. West Coast: Role of atmospheric rivers in extreme precipitation. *Geophys. Res. Lett.*, **44**, 7020–7028, https://doi.org/10.1002/2017GL07419.

——, ——, ——, N. S. Oakley, and J. J. Rutz, 2018: Hourly analyses of the large storms and atmospheric rivers that provide most of California's precipitation in only 10 to 100 hours per year. *San Francisco Estuary Watershed Sci.*, **16**, https://doi.org/10.15447/SFEWS.2018V16ISS4ART1.

Lavers, D. A., M. J. Rodwell, D. S. Richardson, F. M. Ralph, J. D. Doyle, C. A. Reynolds, V. Tallapragada, and F. Pappenberger, 2018: The gauging and modeling of rivers in the sky. *Geophys. Res. Lett.*, **45**, 7828–7834, https://doi.org/10.1029/2018GL079019.

Lin, Y., 2011: GCIP/EOP surface: Precipitation NCEP/EMC 4KM gridded data (GRIB) Stage IV data, version 1.0. UCAR/NCAR Earth Observing Laboratory, accessed 12 March 2019, https://doi.org/10.5065/D6PG1QDD.

Lorenz, E. N., 1969: The predictability of a flow which possesses many scales of motion. *Tellus*, **21**, 289–307, https://doi.org/10.3402/tellusa.v21i3.10086.

Lu, P., N. Lin, K. Emanuel, D. Chavas, and J. Smith, 2018: Assessing hurricane rainfall mechanisms using a physics-based model: Hurricanes Isabel (2003) and Irene (2011). *J. Atmos. Sci.*, **75**, 2337–2358, https://doi.org/10.1175/JAS-D-17-0264.1.

Majumdar, S., 2016: A review of targeted observations. *Bull. Amer. Meteor. Soc.*, **97**, 2287–2303, https://doi.org/10.1175/BAMS-D-14-00259.1.

Martin, J. D., and W. M. Gray, 1993: Tropical cyclone observation and forecasting with and without aircraft reconnaissance. *Wea. Forecasting*, **8**, 519–532, https://doi.org/10.1175/1520-0434(1993)008<0519:TCOAFW>2.0.CO;2.

Martin, A., F. M. Ralph, R. Demirdjian, L. DeHaan, R. Weihs, J. Helly, D. Reynolds, and S. Iacobellis, 2018: Evaluation of atmospheric river predictions by the WRF Model using aircraft and regional mesonet observations of orographic precipitation and its forcing. *J. Hydrometeor.*, **19**, 1097–1113, https://doi.org/10.1175/JHM-D-17-0098.1.

——, ——, A. Wilson, L. DeHaan, and B. Kawzenuk, 2019: Rapid cyclogenesis from a mesoscale frontal wave on an atmospheric river: Impacts on forecast skill and predictability during atmospheric river landfall. *J. Hydrometeor.*, **20**, 1779–1794, https://doi.org/10.1175/JHM-D-18-0239.1.

Neiman, P. J., F. M. Ralph, A. B. White, D. E. Kingsmill, and P. O. Persson, 2002: The statistical relationship between upslope flow and rainfall in California's coastal mountains: Observations during CALJET. *Mon. Wea. Rev.*, **130**, 1468–1492, https://doi.org/10.1175/1520-0493(2002)130<1468:TSRBUF>2.0.CO;2.

——, A. B. White, F. M. Ralph, D. J. Gottas, and S. I. Gutman, 2009: A water vapour flux tool for precipitation forecasting. *Proc. Inst. Civ. Eng. Water Manage.*, **162**, 83–94, https://doi.org/10.1680/wama.2009.162.2.83.

——, B. J. Moore, A. B. White, G. A. Wick, J. Aikins, D. L. Jackson, J. R. Spackman, and F. M. Ralph, 2016: An airborne and ground-based study of a long-lived and intense atmospheric river with mesoscale frontal waves impacting California during CalWater-2014. *Mon. Wea. Rev.*, **144**, 1115–1144, https://doi.org/10.1175/MWR-D-15-0319.1.

Oortwijn, J., and J. Barkmeijer, 1995: Perturbations that optimally trigger weather regimes. *J. Atmos. Sci.*, **52**, 3932–3944, https://doi.org/10.1175/1520-0469(1995)052<3932:PTOTWR>2.0.CO;2.

Orr, W. M., 1907: The stability or instability of the steady motions of a perfect liquid and of a viscous liquid. Part I: A perfect liquid. *Proc. Roy. Irish Acad.*, **27**, 9–68.

Parker, D. J., 1998: Secondary frontal waves in the North Atlantic region: A dynamical perspective of current ideas. *Quart. J. Roy. Meteor. Soc.*, **124**, 829–856, https://doi.org/10.1002/qj.49712454709.

Rabier, F., E. Klinker, P. Courtier, and A. Hollingsworth, 1996: Sensitivity of forecast errors to initial conditions. *Quart. J. Roy. Meteor. Soc.*, **122**, 121–150, https://doi.org/10.1002/qj.49712252906.

Ralph, F. M., 2017: FIRO steering committee co-chairs provide in-depth briefing to USACE. Center for Western Weather and Water Extremes, Scripps Institution of Oceanography, http://cw3e.ucsd.edu/firo-steering-committee-co-chairs-provide-in-depth-briefing-to-usace/.

——, 2018: Atmospheric River Reconnaissance—2018 is underway. Center for Western Weather and Water Extremes, Scripps Institution of Oceanography, http://cw3e.ucsd.edu/atmospheric-river-reconnaissance-2018-underway/.

——, T. Coleman, P. J. Neiman, R. J. Zamora, and M. D. Dettinger, 2013: Observed impacts of duration and seasonality of atmospheric-river landfalls on soil moisture and runoff in coastal Northern California. *J. Hydrometeor.*, **14**, 443–459, https://doi.org/10.1175/JHM-D-12-076.1.

——, J. J. Rutz, J. M. Cordeira, M. Dettinger, M. Anderson, D. Reynolds, L. J. Schick, and C. Smallcomb, 2019: A scale to characterize the strength and impacts of atmospheric rivers. *Bull. Amer. Meteor. Soc.*, **100**, 269–289, https://doi.org/10.1175/BAMS-D-18-0023.1.

Renfrew, I. A., A. J. Thorpe, and C. H. Bishop, 1997: The role of the environmental flow in the development of secondary frontal cyclones. *Quart. J. Roy. Meteor. Soc.*, **123**, 1653–1675, https://doi.org/10.1002/qj.49712354210.

Reynolds, C. A., R. Gelaro, and J. D. Doyle, 2001: Relationship between singular vectors and transient features in the background flow. *Quart. J. Roy. Meteor. Soc.*, **127**, 1731–1760, https://doi.org/10.1002/qj.49712757514.

——, J. D. Doyle, and X. Hong, 2016: Examining tropical cyclone–Kelvin wave interactions using adjoint diagnostics. *Mon. Wea. Rev.*, **144**, 4421–4439, https://doi.org/10.1175/MWR-D-16-0174.1.

——, ——, F. M. Ralph, and R. Demirdjian, 2019: Adjoint sensitivity of North Pacific atmospheric river forecasts. *Mon. Wea. Rev.*, **147**, 1871–1897, https://doi.org/10.1175/MWR-D-18-0347.1.

Rivals, H., J.-P. Cammas, and I. A. Renfrew, 1998: Secondary cyclogenesis: The initiation phase of a frontal wave observed over the eastern Atlantic. *Quart. J. Roy. Meteor. Soc.*, **124**, 243–267, https://doi.org/10.1002/qj.49712454511.

Sawyer, J. S., 1956: The vertical circulation at meteorological fronts and its relation to frontogenesis. *Proc. Roy. Soc. London*, **234A**, 346–362, https://doi.org/10.1098/rspa.1956.0039.

Schemm, S., H. Wernli, and L. Papritz, 2013: Warm conveyor belts in idealized moist baroclinic wave simulations. *J. Atmos. Sci.*, **70**, 627–652, https://doi.org/10.1175/JAS-D-12-0147.1.

Shapiro, M. A., 1981: Frontogenesis and geostrophically forced secondary circulations in the vicinity of jet stream-frontal zone systems. *J. Atmos. Sci.*, **38**, 954–973, https://doi.org/10.1175/1520-0469(1981)038<0954:FAGFSC>2.0.CO;2.

Shoemaker, D. N., W. M. Gray, and J. D. Sheaffer, 1990: Influence of synoptic track aircraft reconnaissance on JTWC tropical cyclone track forecast errors. *Wea. Forecasting*, **5**, 503–507, https://doi.org/10.1175/1520-0434(1990)005<0503:IOSTAR>2.0.CO;2.

Wernli, H., 1997: A Lagrangian-based analysis of extratropical cyclones. II: A detailed case study. *Quart. J. Roy. Meteor. Soc.*, **123**, 1677–1706, https://doi.org/10.1002/qj.49712354211.

——, and H. C. Davies, 1997: A Lagrangian-based analysis of extratropical cyclones. I: The method and some applications. *Quart. J. Roy. Meteor. Soc.*, **123**, 467–489, https://doi.org/10.1002/qj.49712353811.

Winters, A. C., and J. E. Martin, 2014: The role of a polar/subtropical jet superposition in the May 2010 Nashville flood. *Wea. Forecasting*, **29**, 954–974, https://doi.org/10.1175/WAF-D-13-00124.1.

Zhang, Z., F. M. Ralph, and M. Zheng, 2019: The relationship between extratropical cyclone strength and atmospheric river intensity and position. *Geophys. Res. Lett.*, **45**, 1814–1823, https://doi.org/10.1029/2018GL079071.

Zheng, M., E. K. Chang, and B. A. Colle, 2013: Ensemble sensitivity tools for assessing extratropical cyclone intensity and track predictability. *Wea. Forecasting*, **28**, 1133–1156, https://doi.org/10.1175/WAF-D-12-00132.1.